

Investigating the Role of Copper Oxide in Electrochemical CO₂ Reduction in Real Time

Lily Mandal,^{†,‡,§,||} Ke R. Yang,^{||} Mallikarjuna Rao Motapothula,^{†,‡} Dan Ren,^{†,‡,§} Peter Lobaccaro,^{†,∇} Abhijeet Patra,^{‡,§} Matthew Sherburne,^{†,○} Victor S. Batista,^{||} Boon Siang Yeo,^{†,‡,§} Joel W. Ager,^{*,†,§,||,○} Jens Martin,^{*,†,§,||} and T. Venkatesan^{*,†,‡,§,||,◆}

[†]A Singapore Berkeley Research Initiative for Sustainable Energy, Berkeley Educational Alliance for Research in Singapore, 1 CREATE Way, 138602 Singapore

[‡]NUSNNI-Nanocore, National University of Singapore, 117411 Singapore

[§]Department of Physics, National University of Singapore, 117542 Singapore

^{||}Department of Electrical and Computer Engineering, National University of Singapore, 117576 Singapore

[⊥]Centre for Advanced 2D Materials, National University of Singapore, 6 Science Drive 2, 117546 Singapore

[#]Department of Chemistry, Faculty of Science, National University of Singapore, 3 Science Drive 3, 117543 Singapore

[∇]Department of Chemical and Biomolecular Engineering and [○]Department of Materials Science and Engineering, University of California, Berkeley, California 94720, United States

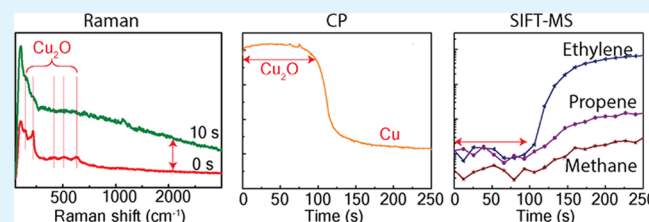
[◆]Department of Integrative Science and Engineering, National University of Singapore, 117456 Singapore

^{||}Yale Energy Sciences Institute and Department of Chemistry, Yale University, New Haven, Connecticut 06520-8107, United States

S Supporting Information

ABSTRACT: Copper oxides have been of considerable interest as electrocatalysts for CO₂ reduction (CO₂R) in aqueous electrolytes. However, their role as an active catalyst in reducing the required overpotential and improving the selectivity of reaction compared with that of polycrystalline copper remains controversial. Here, we introduce the use of selected-ion flow tube mass spectrometry, in concert with chronopotentiometry, in situ Raman spectroscopy, and computational modeling, to investigate CO₂R on Cu₂O nanoneedles, Cu₂O nanocrystals, and Cu₂O nanoparticles. We show experimentally that the selective formation of gaseous C₂ products (i.e., ethylene) in CO₂R is preceded by the reduction of the copper oxide (Cu₂O) surface to metallic copper. On the basis of density functional theory modeling, CO₂R products are not formed as long as Cu₂O is present at the surface because Cu₂O is kinetically and energetically more favorable than CO₂R.

KEYWORDS: electrochemical CO₂ reduction, CO adsorption, chronopotentiometry, Raman spectroscopy, Cu₂O reduction, DFT modeling



1. INTRODUCTION

Conversion of carbon dioxide (CO₂), an important greenhouse gas, into energy-rich chemicals is a viable approach to reducing the global carbon footprint.¹ Electrochemical CO₂ conversion (CO₂R) using renewable electricity is envisaged as a promising technology to achieve this end.^{2–7} Among the many catalysts studied for CO₂R, copper is unique because it is the only metal that reduces CO₂ to significant amounts of C₂ and higher-order hydrocarbons and alcohols.^{8,9} Nanostructuring copper into cubes and needles can enhance the selectivity toward C–C coupled products.^{10–13} Alternatively, copper oxides can be employed as precursors for making high-surface-area structures.^{14–22} When operated under CO₂R conditions (typically –0.8 to –1.1 V vs RHE), the oxides would be reduced to metallic copper (Cu⁰) in accordance with the Pourbaix diagram, producing nanostructured Cu.²³ In the literature, the improved

performance of such oxide-derived copper nanostructures toward C₂ products has been attributed to a number of factors: (1) a higher local pH at the catalyst surface, favoring the pH-independent C–C coupling pathway over the formation of methane,¹³ (2) a higher density of grain boundaries and defect sites, optimizing the binding energy of reaction intermediates such as CO,^{14,20} and (3) the presence of oxides and subsurface oxygen alongside the metal, which provides Cu sites with multiple valences to increase catalytic activity.^{18,19,24}

Studies on copper oxide as a CO₂R electrocatalyst showed transient changes in the product distribution attributed to the temporary presence of surface oxide species.^{21,22} Recently, Li et

Received: October 11, 2017

Accepted: February 13, 2018

Published: February 13, 2018

al. found that thermally oxidized copper showed stable and improved product generation to CO and HCOOH at a lower overpotential compared to that for polycrystalline copper; however, this performance was not attributed to the oxide itself.¹⁵ This is reasonable given the Pourbaix diagram for Cu²³ and was confirmed in their ex situ X-ray diffraction (XRD) study. Kas et al.¹⁷ investigated electrodeposited Cu₂O of different orientation and thickness and found that the selectivity depended on the initial oxide thickness and not on the orientation of the starting copper oxide. By performing cyclic voltammetry and employing online electrochemical mass spectrometry, they concluded that CO₂R starts only after Cu₂O is reduced into Cu. However, this study did not employ an in situ characterization of the catalyst surface. Using in situ Raman spectroscopy, Ren et al. found that in aqueous, CO₂-saturated 0.1 M KHCO₃, the surface of a Cu₂O film reduces within a few minutes to Cu⁰ at negative potentials.¹⁴ Interestingly, in this same study, it was found that when all signals belonging to copper oxide had disappeared, adsorbed CO, the pertinent reaction intermediate in CO₂R, is detected. All of these studies suggest that surface Cu⁰ and not copper oxide is the active catalyst species.

In contrast, Lee et al.¹⁸ and Mistry et al.¹⁹ used in situ X-ray absorption near-edge structure (XANES) spectroscopy to show the presence of Cu⁺ even after CO₂R begins. They proposed that residual Cu⁺ is responsible for the improved selectivity to C₂ products found with oxide-derived (OD) copper. Similarly, Eilert et al.,²⁴ using in situ ambient pressure X-ray photoelectron spectroscopy (XPS), reported the existence of subsurface oxygen during CO₂R. They proposed that the enhanced C₂ selectivity is due to subsurface oxygen, which changes the electronic structure of the Cu and enhances the binding of CO.

However, they concluded that the catalyst is present only in the Cu⁰ state. This contradiction in the results can be explained by the difference in the surface sensitivity of the techniques. XANES is a bulk material characterization technique in contrast to XPS which is a surface-sensitive technique. Mistry et al.¹⁹ and Eilert et al.²⁴ both performed further analysis on the subsurface of the catalyst utilizing transmission electron microscopy energy-dispersive X-ray (TEM-EDX) and transmission electron microscopy electron energy loss spectroscopy (TEM-EELS), respectively, with conflicting conclusions. Mistry et al.¹⁹ claimed that an oxide phase exists, whereas Eilert et al.²⁴ claimed the presence of a pure metallic phase with small subsurface oxide.

Summarizing the current literature,^{15–20} there are conflicting reports regarding the possible role of copper oxide in CO₂R, especially relating to the role of surface copper oxide as the active catalyst. The question remains whether copper oxide itself can be a catalyst,^{18,19} if it only acts as the precursor for the formation of nanostructured copper,^{14–17} or if it could be leaving behind subsurface oxygen that influences the copper's activity.²⁴ Here, we investigate whether surface copper oxide itself plays any role as a catalyst in CO₂R.

Because copper oxides are quickly reduced under cathodic conditions and quickly reoxidized upon the removal of that condition (see Figure S18, Supporting Information (SI) for details), it is difficult to determine with ex situ techniques if the periodically measured products are formed on the oxide or on the (largely) metallic surfaces. In operando, surface-sensitive techniques can help to clarify this.^{25,26} Previously, real-time product detection and in operando surface spectroscopy have

not been combined to investigate the role of copper oxide. Herein, we combine Raman spectroscopy with selected-ion flow tube mass spectrometry (SIFT-MS)^{27–29} to study in real time both the surface and the products generated during electrochemical CO₂R. Density functional theory (DFT) calculations were employed to model the system and could rationalize the results very successfully.

SIFT-MS can detect and quantify gaseous products such as methane, ethane, and ethylene as well as higher-order hydrocarbons, like propene, in a time scale of 0.1–10 s (depending on the number of masses scanned). This enables the capture of reaction dynamics. In this way, it overcomes the classic problem faced in much of the literature where the gaseous products of CO₂R are analyzed by gas chromatography (GC) with analysis times in the range of minutes. In addition, liquid products, typically detected by high-pressure liquid chromatography (HPLC) or nuclear magnetic resonance spectroscopy (NMR), are only measured once at the end of an experiment by sampling aliquots of the electrolyte.^{9,20,25,26,30} SIFT-MS allows the simultaneous detection of liquid products with finite vapor pressure (this aspect of the technique will be presented in another paper). SIFT-MS is able to provide this real-time analysis of complex multicomponent mixtures because of its use of gentle chemical ionization reactions. These reactions, such as proton addition, avoid the fragmentation of molecules typical of electron ionization mass spectrometry (MS), which results in an extremely low limit of detection of the parent ion.²⁶ SIFT-MS has been well reviewed in the literature, and we point the reader to these works^{27–29} for a deeper understanding of the advantages of this technique. We have published technical details of SIFT-MS applied to CO₂R elsewhere.³⁰

Here, three different forms of Cu₂O were synthesized by electrochemical and thermal methods,^{14,15,31} yielding oxide-derived catalysts of different surface structures and different CO₂R activities. These catalysts were subsequently evaluated in real time, using an electrochemical cell previously detailed,³² to determine the onset of CO₂R after switching on a constant cathodic current. By combining DFT study and in situ Raman spectroscopy with real-time product detection, we show that Cu₂O reduction (Cu₂OR) typically occurs before CO₂R begins because Cu₂OR is energetically more favorable. Interestingly, Cu₂O with certain exposed surfaces could be active catalysts for CO₂R if were not poisoned by reaction intermediates.

2. EXPERIMENTAL SECTION

Detailed experimental procedures are given in the [Supporting Information](#).

2.1. Preparation of Catalyst. Three types of copper oxides were prepared for this study. The first was synthesized by thermally annealing copper foils in a tube furnace at 450 °C for 3 h (Cu NPs).¹⁵ Copper oxide nanocrystals (Cu NCs) were synthesized by a method previously reported.¹⁴ Copper oxide nanoneedles (Cu NN) were synthesized by anodizing the Cu foil in 2 M KOH solution in a two-electrode setup using graphite as the counter electrode. The electrode anodization was carried out at a constant current density of 7 mA/cm² for 5 min for synthesizing Cu(OH)₂, after which it was annealed in vacuum at 700 °C to convert Cu(OH)₂ into Cu₂O nanoneedles.³¹

2.2. In Situ Raman Spectroscopy. In situ Raman spectroscopy was carried out with a confocal Raman microscope (modular system from HORIBA Jobin Yvon) in an epi-illumination mode (top-down). A He–Ne laser with 633 nm wavelength (CVI Melles Griot) was used as the excitation source. A water immersion objective lens (LUMFL, Olympus, 60×, numerical aperture: 1.10) covered with a 0.013 mm thin Teflon film (American Durafilm) was used to focus and collect

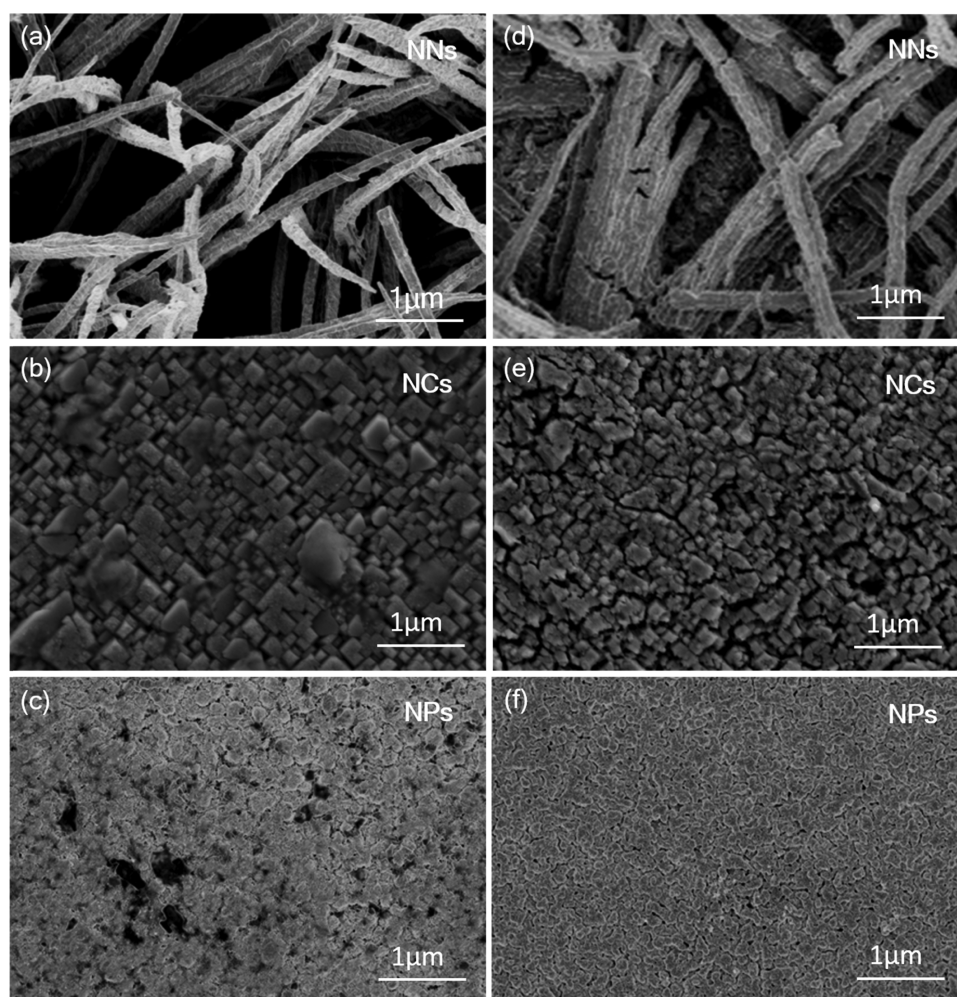


Figure 1. SEM images (scale 1 μm) of as-prepared copper oxides before CO₂R: (a) nanoneedles (NNs), (b) nanocrystals (NCs), and (c) nanoparticles (NPs) and after CO₂R: (d) nanoneedles (NNs), (e) nanocrystals (NCs), and (f) nanoparticles (NPs).

the incident and scattered laser light. The backscattered light was filtered through a 633 nm edge filter, before being directed into a spectrograph (iHR320)/charge-coupled device detector (Synapse CCD). The electrochemical Raman cell was a round Teflon dish with the detachable Cu electrode mounted in the middle.⁵⁰ The acquisition time for each spectrum was 10 s.

2.3. Computational Details. We used the Vienna ab initio simulation package (VASP)^{34–37} for all periodic boundary calculations. The projector augmented wave (PAW)^{38,39} method together with the PBE exchange–correlation functional⁴⁰ was employed to describe the electron–ion interactions. A cutoff of 450 eV was chosen for the plane wave basis set in all calculations. A $5 \times 5 \times 5$ Monkhorst–Pack type k-point grid was chosen for the optimization of bulk Cu and Cu₂O. The Gaussian smear method was used for Cu₂O and Cu. The σ value was chosen to be 0.1 eV for both cases. The energy convergence criterion was set to be 10^{-6} eV per unit cell, and the force convergence criterion of 0.03 eV/Å was used for all structure optimizations. We noted that sometimes the geometry optimization converges to stationary structures rather than energy-minimum structures (Figure S8). Therefore, we optimized all intermediate structures without symmetry constraints and always did frequency calculations to confirm that the optimized structures are energy-minimum structures. For the calculation of transition states (TSs), a tighter convergence criterion of 10^{-8} eV per unit cell was used. We used the nudged elastic band (NEB) method⁴¹ to locate the proper guess TS geometries, which were then optimized to saddle points with the improved dimer method.⁴² Frequency calculations were performed to confirm the nature of located transition states. A $3 \times 3 \times 1$ Monkhorst–Pack type

k-point grid was chosen for slab calculations. Slab models were chosen to have 4 unit cells, which corresponds a coverage of $\theta = 1/4$. Seven layers of Cu were used to construct the Cu(111) slab model, whereas six atomic layers (three layers of Cu and three layers of O) were used to construct the Cu₂O(111) and Cu₂O(200) slab models. The sizes of slab modes were chosen to be $5.13 \text{ Å} \times 5.13 \text{ Å} \times 33.86 \text{ Å}$, $6.084 \text{ Å} \times 6.084 \text{ Å} \times 22.452 \text{ Å}$, and $6.084 \text{ Å} \times 6.084 \text{ Å} \times 23.605 \text{ Å}$ for the Cu(111), Cu₂O(111), and Cu₂O(200) surfaces, respectively. During the geometry optimization of the slab models, bottom five layers of Cu(111) slabs and bottom two layers (one layer of Cu and one layer of O) of Cu₂O(111) and Cu₂O(200) slabs were fixed at the bulk position.

The relative energies of intermediates of CO₂ reduction (CO₂R), hydrogen evolution reaction (HER), and Cu₂O reduction (Cu₂OR) were calculated relative to CO₂, H₂, and bare surfaces. For reactions involving the release of H₂O, e.g., *COOH to *CO, the energy of isolated H₂O was used in the calculations. A supercell of $15.0 \text{ Å} \times 15.0 \text{ Å} \times 15.0 \text{ Å}$, the Gaussian smearing method and a σ value of 0.1 eV were used in the calculations of small molecules. For reaction steps involving H⁺ and e[−], the computational hydrogen electrode technique developed by Nørskov et al.⁴³ was used to consider the dependence of relative energies on pH and applied bias potential and the detailed calculation approach is shown in Scheme S1 (see computational details in SI). The dispersion interactions were considered with Grimme's D3 correction,⁴⁴ and the solvation effects were considered with the implicit solvation model as implemented in VASPsol.⁴⁵ A dielectric constant of 80.0 was used to represent bulk water solvent. The effects of dispersion and solvation are shown in Figures S9–S11. Frequency

analysis was performed for both absorbates and surface atoms, which are allowed to relax to calculate thermal correction to the free energies, which are listed in Tables S4–S7. Please refer the Supporting Information for more computational details.

3. RESULTS AND DISCUSSION

3.1. Characterization of Electrocatalysts. Scanning electron microscopy (SEM) images of catalyst precursor structures formed from nanoneedles (NNs), cubic nanocrystals (NCs), and nanoparticles (NPs) before and after CO₂R are shown in Figure 1a–f. Clearly, the morphology of all catalysts after reduction is different and different from that of the pristine Cu₂O state (also distinct from planar electropolished Cu; Figure S2). In particular, we note that the reduced catalysts appeared to be composed of small particles, which could increase the effective catalytic area and provide a variety of defects and step-edge sites. Figure 2a,c,e shows the XRD

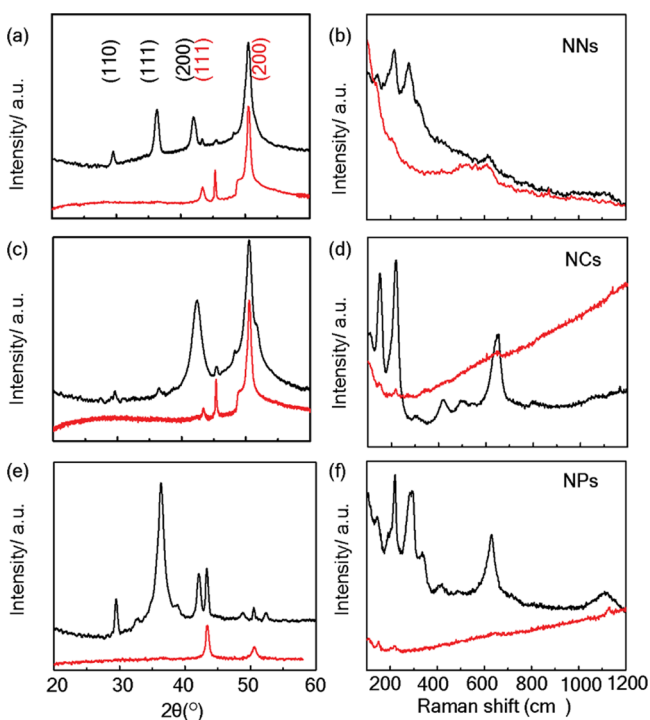


Figure 2. XRD patterns of copper oxide before (black) and after CO₂R (red): (a) NNs, (c) NCs, and (e) NPs showing peaks corresponding to Cu₂O (black) and underlying Cu substrate (red). Raman spectra of copper oxide before (black) and after CO₂R (red): (b) NNs, (d) NCs, and (f) NPs showing peaks corresponding to Cu₂O (109, 152, 415, 645), CuO (303, 634), and Cu(OH)₂ (490).

patterns of the copper oxide samples before and after CO₂R. In all samples before CO₂R, we can identify peaks corresponding to Cu₂O and the underlying Cu substrate in accordance with database patterns extracted from the International Center for Diffraction Data (ICDD No-01-077-0199 for Cu₂O and 00-004-0836 for Cu). The Cu₂O samples have different preferential orientations, shown by the higher intensities of the (200) peak of NCs versus those of the (111) peak of NPs. Interestingly, all three catalysts showed different preferential orientations after reduction as well; NCs and NNs showed higher intensities of the Cu (200) peak versus those of the Cu (111) peak of NPs.

The Raman spectra collected under ambient conditions before and after CO₂R are shown in Figure 2b,d,f, and the identified Raman peaks are listed in Table S1. Interestingly, NN and NP samples show Cu₂O peaks slightly below Γ_{12}^- at 109 cm⁻¹ and $\Gamma_{15}^{(1)}$ at 154 cm⁻¹ possibly due to defect formation or strain. In contrast, the NC sample shows Cu₂O peaks close to the expected values and with low Raman intensity. In perfect crystals, Γ_{12}^- and $\Gamma_{15}^{(1)}$ phonon modes are IR-active and Raman-inactive.⁴⁶

In the following sections, we investigate the initial period of Cu-oxide reduction in more detail employing in situ spectroscopic methods and DFT modeling.

3.2. In Situ Measurement of CO₂R Products. A benchmark study was performed to validate that the CO₂R production measurements made by SIFT-MS agree with those performed with traditional techniques such as GC (see Figure S1 for the experimental setup). The products from copper oxide NNs operated at a constant current density of -10 mA/cm² were measured. Figure 3a shows the GC data and overlaid SIFT-MS data for methane, ethylene, and propene (SIFT-MS detects all hydrocarbons but cannot detect H₂ and CO). The extracted Faradaic efficiency (FEs) of both methods coincided within experimental uncertainties. Additional comparative data for SIFT and GC are provided in the SI (Figure S4). Figure 3b shows the real-time measurement of FEs for methane (C₁), ethylene (C₂), and propene (C₃). As explained below, during the first few minutes, Cu₂O reduction predominates, and we do not observe the CO₂R product in SIFT-MS. The sensitivity of the SIFT-MS technique is evident from the detection of the C₃ product with only 0.1% FE. Detailed FEs of the products are listed in SI (Table S2).

Once a current is applied to a Cu₂O cathode, three reduction processes are possible, namely, CO₂R, hydrogen evolution reaction (HER), and Cu₂O to metallic copper. To identify the dominant reaction in the initial phase, we take advantage of the real-time sensitivity of SIFT-MS. Figure 4 shows the

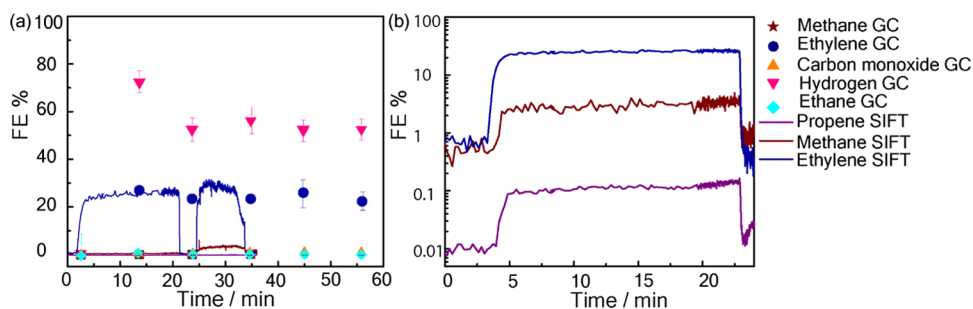


Figure 3. (a) Comparison of GC (points) and SIFT-MS (lines) data from Cu NNs operated at -10 mA/cm² in 0.1 M KHCO₃. (b) Semi-log plot of SIFT data for methane (C₁), ethylene (C₂), and propene (C₃).

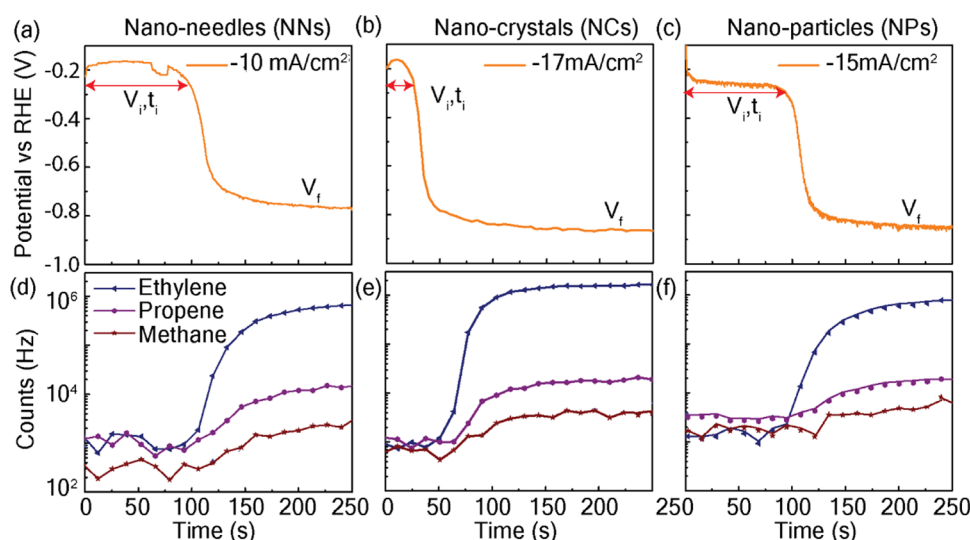


Figure 4. CP (top) and SIFT-MS (bottom) data of Cu_2O (a, d) NNs driven at -10 mA/cm^2 , (b, e) NCs driven at -17 mA/cm^2 , and (c, f) NPs driven at -15 mA/cm^2 , all in 0.1 M KHCO_3 electrolyte saturated with 1 atm CO_2 . The SIFT-MS data is corrected for its intrinsic response time (see SI-II, Figure S3).

chronopotentiometry (CP) and online SIFT-MS data of the different samples (the liquid products are shown in Figure S5). In a CP measurement, constant current is applied to an electrochemical cell and the change in voltage is measured as a function of time. Different current densities are chosen for different samples such that the long-term potential for all samples is approximately -0.8 V versus the reversible hydrogen electrode (RHE), a good operational condition for CO_2R .^{14,15} The CP curve for all samples possesses a slightly negative initial potential ($V_i \approx -0.2 \text{ V}$ vs RHE) up to a time (t_i) when the potential steeply increases to stabilize at a final potential ($V_f \approx -0.8 \text{ V}$). The observed change in potential from V_i to V_f is due to the change in the surface reaction at the cathode from copper oxide reduction during V_i , t_i to CO_2R after that and is explained in detail in SI-V. Time traces for NC samples run at different current densities are shown in the SI (Figure S6). In all cases, CO_2R products are detected only after the increase in the overpotential measured in CP. This provides strong evidence that at the beginning Cu_2OR is kinetically favored relative to CO_2R . Only when Cu-oxide is essentially completely reduced to metal does CO_2R begin.

Because SIFT-MS cannot detect CO and H_2 , we have conducted GC measurements to rule out HER during the initial phase. Because of the slow time evolution of GC, we slowed down the rate of Cu_2O reduction to stretch the initial phase t_i . Hence, we have run the samples at a very low constant current density of -1 mA/cm^2 . Figure 5 shows the chronopotentiometry and GC data of NCs and NNs under such conditions, confirming that there are no HER and no CO_2R products (including CO and H_2) during the initial period, t_i . Cu NPs run at -1 mA/cm^2 did not fully reduce during the 1 h reaction, and no products are observed by GC shown in the SI (Figure S7).

3.3. Density Functional Theory Modeling. To rationalize the distinct reactivity of Cu_2O NCs, NNs, and NPs, we analyzed the reaction free energy profiles of CO_2R at the density functional theory (DFT) level, using the Vienna ab initio simulation package.^{34–37} Figure 2 shows that the dominant XRD peak of Cu_2O NPs corresponds to the (111) surface and that of Cu_2O NCs corresponds to the (200) surface, whereas those of Cu_2O NNs exhibit both (111) and

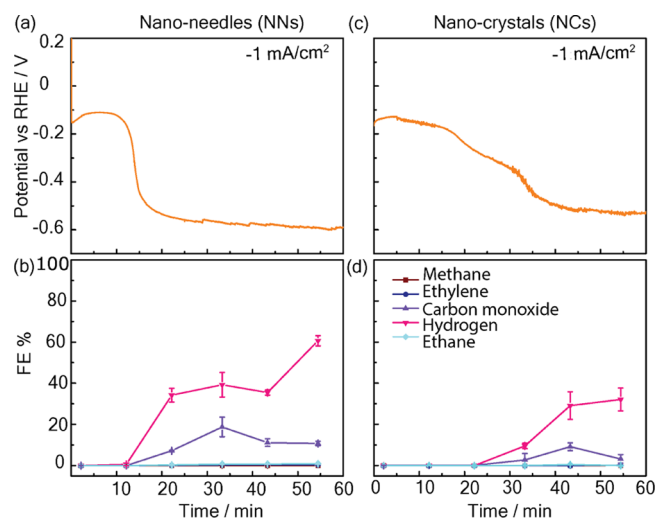


Figure 5. Evolution of CO and H_2 at low current density: (a) NC chronopotentiometry, (b) NN chronopotentiometry, (c) NC GC data, and (d) NN GC application of current; GC data show only negligible amount of data evolution of CO and H_2 during the first $10\text{--}20 \text{ min}$ when Cu_2OR prevails in the 0.1 M KHCO_3 electrolyte saturated with 1 atm CO_2 .

(200) surfaces. Therefore, we calculated the relative free energies of intermediates of CO_2R , HER, and Cu_2OR on both Cu_2O (111) and Cu_2O (200) relative to CO_2 , H_2 , and bare surfaces. In addition, we computed the relative free energies of intermediates of HER and CO_2R on Cu (111).

Figure 6a shows the DFT-optimized geometries of model surfaces of Cu (111), Cu_2O (111), and Cu_2O (200). The Cu–Cu distance on Cu (111) is 2.57 \AA , similar to that of bulk Cu. In contrast, the Cu atoms on Cu_2O (111) and Cu_2O (200) are significantly spaced more due to their coordination to O atoms (Figure S8). In addition, the presence of subsurface O atoms creates different binding sites, leading to different binding modes and reactivity of molecular adsorbates. For example, with the PBE functional, CO prefers to bind at fcc sites on the Cu (111) surface, with a binding energy of -0.79 eV , consistent with previous studies.⁴⁷ However, as shown in Figure S8, on the

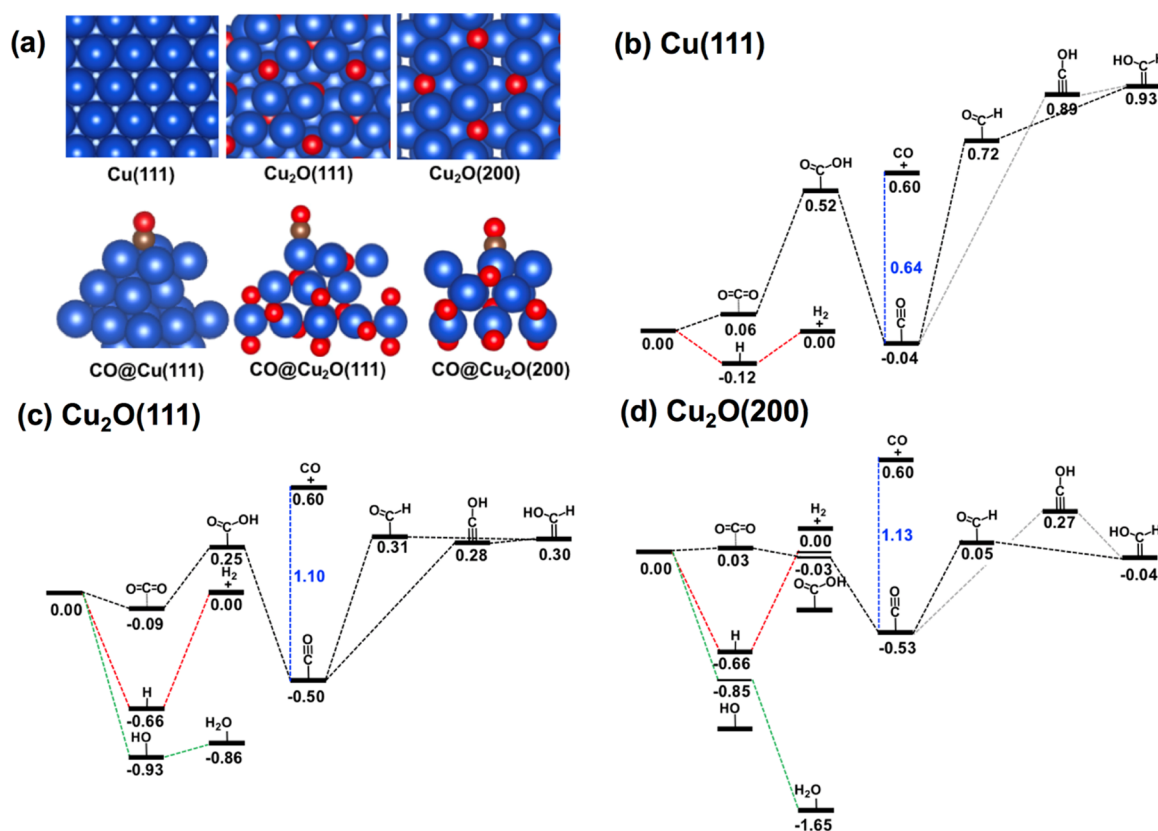


Figure 6. DFT-optimized geometries and relative free energies of intermediates of HER (red dash line), CO₂R (black dash line), and Cu₂OR (green dash line) on Cu (111), Cu₂O (111), and Cu₂O (200) relative to CO₂, H₂, and bare surfaces. (a) DFT-optimized surfaces of Cu(111), Cu₂O(111), and Cu₂O (200) and CO absorption geometries at the fcc site of Cu (111), Cu atop site of Cu₂O (111), and bridge site of Cu₂O (200). Calculated binding free energies of intermediates on (b) Cu(111), (c) Cu₂O(111), and (d) Cu₂O(200) surfaces [in eV].

Cu₂O (111) surface, CO prefers to bind at the atop position of Cu atoms (−1.37 eV) and on the Cu₂O (200) surface, CO binds at the bridge site (−1.34 eV), forming stronger bonds than on Cu (111).

We first analyze the HER and CO₂R on Cu (111). Figure 6b shows the relative free energies of intermediates of HER and CO₂R. The reduction of protons to form surface-bound hydrogen atoms is energetically favorable, and the subsequent reduction to release H₂ requires only 0.12 eV, consistent with the experimental observation that hydrogen is the major product at low bias potentials.⁴⁸ The reduction of CO₂ to CO needs to overcome the high-energy intermediate *COOH with a relative free energy of 0.52 eV, whereas further reduction of CO needs to overcome the high-energy intermediate *CHO with an energy increase of 0.76 eV. Both energy uphill steps involve redox processes, which can thus be driven by applying a potential. As shown in Figure S12, the total energy balance for CO reduction products becomes negative when applying a bias potential more negative than −0.76 eV, yielding an estimated onset potential consistent with previous experiments⁴⁸ and computations.⁴⁹

Next, we analyze the reduction of Cu₂O surfaces through Cu₂OR and CO₂R reaction pathways. Figure 6c,d shows the relative free energies of the intermediates of HER, CO₂R, and Cu₂OR on Cu₂O (111) and Cu₂O (200). As mentioned above, CO binds more strongly on Cu₂O surfaces than on Cu (111). In addition, all other intermediates of CO₂ reduction are more stabilized on Cu₂O surfaces. Furthermore, the reduction of a proton to form surface-bound hydrogen is energetically very

favorable on Cu₂O (111), more favorable than CO₂R pathways. However, the reduction of the second proton to release H₂ requires an energy increase of 0.66 eV. The reduction of a subsurface O atom to form surface-bound OH on Cu₂O (111) is energetically very favorable, but the further reduction of surface-bound OH to H₂O is slightly energy uphill. With bias potentials more negative than −0.07 V, it is possible to open a Cu₂OR pathway to reduce surface-bound hydroxyl groups to H₂O (Figure S13a). At an even more negative bias potential (<−0.78 V), the reduction of surface-bound CO is also possible, leading to hydrocarbon products (Figure S13c). Similar energetics applies to Cu₂O (200) (Figure S14). Again, the reduction of subsurface O atoms to form surface-bound hydroxyl groups, and ultimately H₂O, is very favorable. We note that the binding location for H and OH differ (Figure S8), and consequently, the strong binding energy of H does not hinder Cu₂OR. Thus, Cu₂OR on Cu₂O (200) is more favorable than the HER or CO₂R and it is the expected reaction to proceed (for energy diagrams under bias, see Figure S14). We note that the reduction of surface-bound CO on Cu₂O (200) requires much less energy than on Cu(111), suggesting that CO₂R on Cu₂O(200) is possible. However, the Cu₂OR is energetically favorable and expected to be the dominant reaction. For completeness, we also highlight that a surface oxygen atom is easily removed from Cu surfaces (Figure S15).

The calculated energetics suggests that Cu₂OR is thermodynamically more favorable than CO₂R on both Cu₂O(111) and Cu₂O(200). We also located transition states associated with Cu₂OR and CO₂R on both surfaces, and the results are given

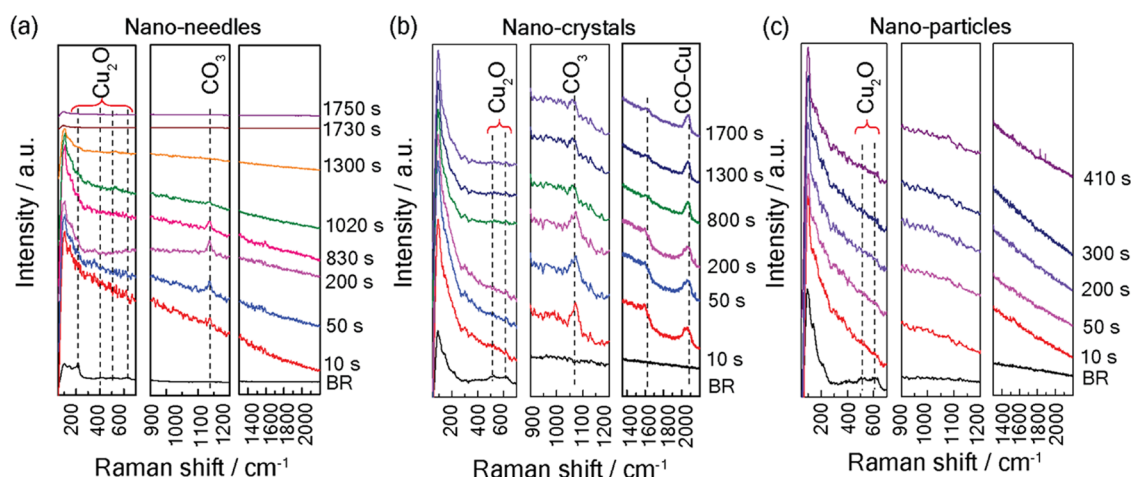


Figure 7. In operando Raman spectroscopy runs at 10 s integration each with a constant current density of -1 mA/cm^2 in CO_2 -saturated 0.1 M KHCO_3 solution for (a) Cu_2O nanoneedles, (b) Cu_2O nanocrystals, and (c) Cu_2O nanoparticles. Each Raman spectrum is divided into three parts to display the Cu_2O , carbonate, and Cu-CO Raman bands.

in Figure S16. The barriers for Cu_2OR are much lower than those for CO_2R . Therefore, Cu_2OR is both energetically and kinetically more favorable than CO_2R on both copper oxide surfaces.

3.4. In Situ Raman Spectroscopy. We now discuss in situ Raman spectra for the different copper oxide samples. Figure 7b shows the time-dependent Raman spectra of NCs (the corresponding CP curves are shown in Figure S17). The black curve was taken as reference and is measured in the original condition before the reaction has started (no current is applied). We can identify peaks at 144, 215, 528, and 623 cm^{-1} corresponding to Cu_2O .⁵⁰ After application of current, the next Raman spectrum is taken at 10 s, and it shows a significant enhancement in intensity. The signal enhancement can be due to either surface-enhanced Raman spectroscopy (SERS)³³ or inelastic light scattering by charge carrier excitations in the metal (i.e., by electron-hole pair excitations), which are made possible by the breakdown in momentum conservation caused by the submicroscopic surface roughness.⁵¹ Considering that enhancement in Raman spectra (RS) is observed, we conclude that a metal Cu layer forms as Cu_2O reduction starts, whereas residual oxide remains present in the bulk. With enhancement in RS, there is a corresponding change in the background signal, making it hard to interpret the peaks in the range of $100\text{--}250 \text{ cm}^{-1}$. Hence, we focus on Cu_2O peaks between 250 and 750 cm^{-1} . After the current is applied, the Raman peaks attributed to Cu_2O (528 and 623 cm^{-1}) show a sudden decrease in the intensity. Furthermore, there are indications of Cu defect-related peaks in the region of $100\text{--}250 \text{ cm}^{-1}$.³³ These observations are consistent with an immediate formation of a metallic Cu surface layer once current is applied. The limits of detection of our Raman spectroscopy measurements do not allow us to determine if there could be trace amounts of residual O atoms embedded in the catalysts.

The Raman spectra provide additional information on CO_2R reaction intermediates. Figure 7b shows the instantaneous appearance of new peaks at 1074 and 2060 cm^{-1} after the application of current. The 1074 cm^{-1} peak is attributed to the stretching mode of adsorbed CO_3^{2-} ($\text{CO}_{3\text{ad}}$)^{52,53} (the bicarbonate deprotonates after adsorption) consistent with the observation of Xu et al.,^{54,55} Hori et al.,⁵⁶ and Wuttig et al.⁵⁷ The adsorbed carbonate is the surface-adsorbed species and

does not participate in the CO_2R . When electrochemical CO_2R is performed in an Ar-purged bicarbonate solution, no CO_2R products are generated; thus, there is no possibility of electroreduction of bicarbonate (i.e., bicarbonate as active species in CO_2R). In a recent report, Dunwell et al.⁵⁴ used in situ spectroscopy and isotopic labeling to show that bicarbonate increases the reducible CO_2 concentration (dissolved CO_2) in the solution through rapid equilibrium exchange between aqueous CO_2 and bicarbonate near the electrode surface. For Cu NC samples, we see the decrease in the concentration of CO_3^{2-} near the surface with time. This can be assigned to the increase in potential (see Figure S6a), as higher negative electrode potentials decrease the adsorption of anions. The peak at 2060 cm^{-1} is attributed to adsorbed CO.^{57–60} Whereas Raman spectra show the appearance of CO on NCs within seconds after the application of current, the corresponding GC data shows only negligible production of CO, H_2 , or any other hydrocarbons during the first 20 min (Figure 5a,b). The applied current density of -1 mA/cm^2 corresponds to a very low potential, which cannot reduce CO further. However, for Cu_2O NCs, with dominant (200) surfaces exposed, Cu_2OR can occur at a very low potential, as shown by our DFT calculation. Hori et al.⁶⁰ have shown that adsorbed CO suppresses hydrogen generation and other electrochemical reductions. Indeed, the rate-determining step in CO_2R is the step following CO adsorption.^{58–61} Thermodynamic analysis shows that high coverage of CO blocks hydrogen absorption sites, inhibiting C–H bond formation.^{62,63} Our DFT calculations show that Cu_2OR is energetically the most favorable reaction pathway, but with the Cu site blocked by CO, CO_2R and HER have also a dynamic disadvantage. Consequently, Cu_2OR will dominate until almost all of the oxide is reduced.

Figure 7a,c shows the Raman spectra of NNs and NPs, respectively. Consistent with our observations on NCs, we find quasi-instantaneous reduction of copper oxide-related peaks within the first few seconds, confirming the formation of copper. Interestingly, the three copper oxide samples differ in terms of the bicarbonate and adsorbed CO peaks. Compared with NCs, the NNs show a very weak CO peak, whereas NPs do not show any adsorbed CO peaks. As shown in Figure 1, all of the three catalysts on reduction generate different nanostructures with different defect densities and preferential

crystal orientations, as shown by the higher intensities of the (200) peak of NCs versus those of the (111) peak of NPs. Consequently, under-coordinated sites, such as defects and boundaries, are expected to be different in all three catalysts. The difference in the intensities of the CO peak can be related to the adsorption strength of CO on these different defects and crystal orientation. This is also evident by the difference in product distribution on the three catalysts shown in Table S2. A direct quantitative comparison of the selectivity and efficiency of these SERS-active Cu films (Cu NC, Cu NN, and Cu NP) relative to each other is not possible as the SERS intensity is convoluted with the different surface structures of the reduced Cu. We nonetheless observe that Cu NC and Cu NN samples are capable of producing higher-order C2–C3 products such as propylene (detected by SIFT-MS) and propanol (detected by head space GC) compared with the Cu NP sample (see Tables S2 and S3). This is consistent with the more intense adsorbed CO peak in the Raman spectra shown in Figure 7a,b. For the Cu NC sample, we observed the inhibition of the catalyst surface to liberate the electrogenerated CO. This indicates that there could be a high population of surface-adsorbed CO, which is necessary for conversion to higher-order products.⁵⁶

To empirically validate the claim that essentially all Cu₂O is reduced within the initial time, t_i , we estimate the effective thickness of reduced Cu₂O on the basis of the partial current density for Cu₂O reduction. On the basis of our experimental findings, we assume that all current goes to Cu₂O reduction until CO₂R or HER products are detected. Afterward, the measured CO₂R and HER contributions are subtracted from the total current to find the current still going toward Cu₂O reduction. For this estimate, we use NCs because of their simplified morphology (Figures 1b and S19a). Figure 3c shows that within the first 54 s there is no change in the SIFT background signal; thus, all applied current is assumed to be consumed by Cu₂O. The calculated thickness of the reduced Cu₂O layer is $1.1 \pm 0.1 \mu\text{m}$, which is consistent with the estimated thickness of Cu₂O in the NC samples of $1.2 \pm 0.1 \mu\text{m}$, as determined by cross-sectional SEM (Figure S19a).

In a second estimation, we use data from the much lower current density experiments (Figure 4a,b). Within the initial time ($t_i = 700 \text{ s}$), an estimated 860 nm of Cu₂O is reduced, which is less than the estimated total thickness of the Cu₂O layer from SEM images. However, we note that the Cu₂O peaks disappear from the Raman spectra within 10 s of applying a potential; thus, the reduction must proceed from the surface deeper into the bulk of the catalyst. Therefore, the residual copper oxide yet to be reduced must be present in the bulk of the catalyst. This leaves open the possibility that Cu₂O reduction continues at a lower rate in the bulk in parallel to CO₂R and HER at the surface once the potential has increased (Figure S20). With this assumption, we calculate that all of the Cu₂O is completely reduced to Cu within 20 min, similar to the observations by Lee et al. and Mistry et al. A similar calculation for the Cu NP sample is given in SI-X.

Oxide-derived Cu nanostructures can easily reoxidize under OCP conditions, as shown in Figure S17 and by Lum et al.,⁶⁴ compromising the ex situ measurement. From the reduction of Cu₂O peaks and the apparent noise level in the after-CO₂R XRD spectra, we can estimate an upper bound of residual crystalline Cu₂O of 3%. By comparing the heights of residual Cu₂O-related peaks in Raman spectra, we can estimate an upper bound of 6% of Cu₂O. In contrast to XRD that measures the bulk, Raman spectroscopy is more surface-sensitive, which

explains the larger estimate for residual Cu₂O. Considering a typical thickness of 4 nm of natural Cu₂O, we conclude that residual Cu₂O is not more than 6%, consistent with recent studies.⁶⁴

The high C2 (ethylene)/C3 (propane, propanol) product selectivity exhibited by these catalysts is due to the higher defect density in these catalysts supporting adsorption of CO, as shown by Ren et al.¹⁴ and Li et al.¹⁵ Furthermore, the OD Cu has high geometrical surface area (because of the nanostructure), leading to high local current density. During CO₂R and HER, protons from water are consumed and OH⁻ ions are released at the electrode surface, increasing the local pH near the electrode surface. The high local pH favors C–C coupling at low overpotential versus RHE, as shown by Koper et al.⁶³ and Lum et al.⁶⁵ The high local pH on the catalyst surface favors the CO dimerization pathway for ethylene formation. It should be noted that in situ SIFT-MS and the limits of detection of our Raman spectroscopy measurements do not allow us to determine if there could be trace amounts of residual O atoms embedded in the catalysts, as reported earlier by Nilsson et al.^{24,66} and Favaro et al.^{67,68} We highlight here though that copper oxides are extremely prone to be reduced to Cu metal at the potentials used in this work.²³ Hence, we believe that if there is any residual O it should be in the bulk rather than on the surface.

4. CONCLUSIONS

In summary, by operando SIFT-MS, computational modeling, and Raman spectroscopy, we show that in three oxide-derived Cu electrocatalysts, with differing surface morphologies and crystal orientations, surface copper oxide reduces prior to CO₂R into gaseous products. Even though Cu₂O (200) seems to be a possible catalyst for CO₂R based on our DFT modeling, CO₂R products are not formed as long as Cu₂O is present at the surface because Cu₂O is kinetically and energetically more favorable than CO₂R. Although we cannot exclude a small percentage of residual oxygen (as has been claimed by Favaro et al.²⁴), it is unlikely that it will be present in the form of Cu₂O. Looking forward, the exceptional performance of SIFT-MS for real-time electrochemical CO₂R can offer new applications in time-resolved monitoring of reaction intermediates.

■ ASSOCIATED CONTENT

§ Supporting Information

The Supporting Information is available free of charge on the ACS Publications website at DOI: 10.1021/acsami.7b15418.

Experimental procedures; computational details; schematic of the whole setup; dead time of the SIFT-MS; chronopotentiometry in operando SIFT-MS data on electropolished Cu; SEM images of electropolished Cu before and after CO₂R; Raman peaks of copper oxide samples; comparative data for SIFT and GC for polycrystalline copper; Cu₂O NNs, NCs, and NPs; FE of the product measured using GC, head space GC, and HPLC; Cu₂O NCs run in SIFT-MS at different current densities; FE of CO₂R products measured using GC, head space GC, and HPLC for nanoneedles and nanocrystal run at -1 mA/cm^2 ; chronopotentiometry and GC data of Cu₂O NPs run at -1 mA/cm^2 ; binding geometries and energies of H, CO, and H–O_{Cu₂O} on Cu₂O surfaces; binding energies of intermediates on Cu

and Cu₂O surfaces; thermal corrections of intermediates; relative free energies at different bias potentials; free energy to remove O atoms on Cu(111); geometries of transition states for Cu₂OR and CO₂R on Cu₂O surfaces and associated barrier height; chronopotentiometry curve for in operando Raman spectroscopy; in situ Raman spectra of Cu NCs; cross-sectional SEM image of Cu₂O NCs; thickness calculation for Cu₂O NCs; coordinates of all intermediates in the VASP format (PDF)

AUTHOR INFORMATION

Corresponding Authors

*E-mail: jwager@berkeley.edu (J.W.A.).

*E-mail: phyjm@nus.edu.sg. Phone: (65) 6516 4140 (J.M.).

*E-mail: venky@nus.edu.sg. Phone: (65) 6516 5187 (T.V.).

ORCID

Lily Mandal: 0000-0001-9010-2403

Dan Ren: 0000-0003-3738-6421

Abhijeet Patra: 0000-0003-0422-3319

Victor S. Batista: 0000-0002-3262-1237

Boon Siang Yeo: 0000-0003-1609-0867

Joel W. Ager: 0000-0001-9334-9751

Author Contributions

The manuscript was written through contributions of all authors. All authors have given approval to the final version of the manuscript. K.R.Y. and M.R.M. contributed equally.

Notes

The authors declare no competing financial interest.

ACKNOWLEDGMENTS

This work was supported by the Singapore National Research Foundation under its Campus for Research Excellence and Technological Enterprise (CREATE) program through the Singapore-Berkeley Research Initiative for Sustainable Energy (SinBeRISE). M.M. is supported by NUSNNI-Nanocore, J.M. is supported by the Centre for Advanced 2D Materials supported by the National Research Foundation, Prime Minister's Office, Singapore, under its Medium Size Centre program. B.S.Y. and D.R. are supported by an academic research grant from National University of Singapore (R-143-000-683-112). D.R. acknowledges the PhD Research Scholarship from Ministry of Education, Singapore. K.R.Y. and V.S.B. acknowledge computer time from National Energy Research Supercomputing Center (NERSC) and funding from Air Force Office of Scientific Research Grant FA9550-17-0198.

ABBREVIATIONS

CO₂R, carbon dioxide reduction

Cu₂OR, copper oxide reduction

CP, chronopotentiometry

GC, gas chromatography

SIFT-MS, selected-ion flow tube mass spectrometry

HER, hydrogen evolution reaction

FE, Faradaic efficiency

REFERENCES

(1) Graves, C.; Ebbesen, S. D.; Mogensen, M.; Lackner, K. S. Sustainable hydrocarbon fuels by recycling CO₂ and H₂O with renewable or nuclear energy. *Renewable Sustainable Energy Rev.* **2011**, *15*, 1–23.

(2) Zhu, D. D.; Liu, J. L.; Qiao, S. Z. Recent Advances in Inorganic Heterogeneous Electrocatalysts for Reduction of Carbon Dioxide. *Adv. Mater.* **2016**, *28*, 3423–3452.

(3) Kumar, B.; Brian, J. P.; Atla, V.; Kumari, S.; Bertram, K. A.; White, R. T.; Spurgeon, J. M. New trends in the development of heterogeneous catalysts for electrochemical CO₂ reduction. *Catal. Today* **2016**, *270*, 19–30.

(4) Lu, Q.; Rosen, J.; Jiao, F. Nanostructured Metallic Electrocatalysts for Carbon Dioxide Reduction. *ChemCatChem* **2015**, *7*, 38–47.

(5) Jones, J.-P.; Prakash, G. K. S.; Olah, G. A. Electrochemical CO₂ Reduction: Recent Advances and Current Trends. *Isr. J. Chem.* **2014**, *54*, 1451–1466.

(6) Qiao, J.; Liu, Y.; Hong, F.; Zhang, J. A review of catalysts for the electroreduction of carbon dioxide to produce low-carbon fuels. *Chem. Soc. Rev.* **2014**, *43*, 631–675.

(7) Costentin, C.; Robert, M.; Savéant, J.-M. Catalysis of the electrochemical reduction of carbon dioxide. *Chem. Soc. Rev.* **2013**, *42*, 2423–2436.

(8) Hori, Y. In *Modern Aspects of Electrochemistry*; Vayenas, C. G., White, R. E., Gamboa-Aldeco, M. E., Eds.; Springer: New York, 2008; Vol. 42, pp 89–189.

(9) Kuhl, K. P.; Cave, E. R.; Abram, D. N.; Jaramillo, T. F. New insights into the electrochemical reduction of carbon dioxide on metallic copper surfaces. *Energy Environ. Sci.* **2012**, *5*, 7050–7059.

(10) Reske, R.; Mistry, H.; Behafarid, F.; Cuenya, B. R.; Strasser, P. Particle Size Effects in the Catalytic Electroreduction of CO₂ on Cu Nanoparticles. *J. Am. Chem. Soc.* **2014**, *136*, 6978–6986.

(11) Roberts, F. S.; Kuhl, K. P.; Nilsson, A. High selectivity for ethylene from carbon dioxide reduction over copper nanocube electrocatalysts. *Angew. Chem.* **2015**, *127*, 5268–5271.

(12) Zhao, Y.; Wang, C.; Wallace, G. G. Tin nanoparticles decorated copper oxide nanowires for selective electrochemical reduction of aqueous CO₂ to CO. *J. Mater. Chem. A* **2016**, *4*, 10710–10726.

(13) Roberts, F. S.; Kuhl, K. P.; Nilsson, A. Electroreduction of Carbon Monoxide Over a Copper Nanocube Catalyst: Surface Structure and pH Dependence on Selectivity. *ChemCatChem* **2016**, *8*, 1119–1124.

(14) Ren, D.; Wong, N. T.; Handoko, A. D.; Huang, Y.; Yeo, B. S. Mechanistic Insights into the Enhanced Activity and Stability of Agglomerated Cu Nanocrystals for the Electrochemical Reduction of Carbon Dioxide to n-Propanol. *J. Phys. Chem. Lett.* **2016**, *7*, 20–24.

(15) Li, C. W.; Kanan, M. W. CO₂ reduction at low overpotential on Cu electrodes resulting from the reduction of thick Cu₂O films. *J. Am. Chem. Soc.* **2012**, *134*, 7231–7234.

(16) Li, C. W.; Ciston, J.; Kanan, M. W. Electroreduction of carbon monoxide to liquid fuel on oxide-derived nanocrystalline copper. *Nature* **2014**, *508*, 504–507.

(17) Kas, R.; Kortlever, R.; Milbrat, A.; Koper, M. T. M.; Mul, G.; Baltrusaitis, J. Electrochemical CO₂ reduction on Cu₂O-derived copper nanoparticles: controlling the catalytic selectivity of hydrocarbons. *Phys. Chem. Chem. Phys.* **2014**, *16*, 12194–12201.

(18) Lee, S.; Kim, D.; Lee, J. Electrocatalytic Production of C3–C4 Compounds by Conversion of CO₂ on a Chloride-Induced Bi-Phase Cu₂O–Cu Catalyst. *Angew. Chem.* **2015**, *127*, 14914–14918.

(19) Mistry, H.; Varela, A. S.; Bonifacio, C. S.; Zegkinoglou, I.; Sinev, I.; Choi, Y.-W.; Kisslinger, K.; Stach, E. A.; Yang, J. C.; Strasser, P.; Cuenya, B. R. Highly selective plasma-activated copper catalysts for carbon dioxide reduction to ethylene. *Nat. Commun.* **2016**, *7*, 12123.

(20) Verdager-Casadevall, A.; Li, C. W.; Johansson, T. P.; Scott, S. B.; McKeown, J. T.; Kumar, M.; Stephens, I. E. L.; Kanan, M. W.; Chorkendorf, I. Probing the Active Surface Sites for CO Reduction on Oxide-Derived Copper Electrocatalysts. *J. Am. Chem. Soc.* **2015**, *137*, 9808–9811.

(21) Le, M.; Ren, M.; Zhang, Z.; Sprunger, P. T.; Kurtz, R. L.; Flake, J. C. Electrochemical Reduction of CO₂ to CH₃OH at Copper Oxide Surfaces. *J. Electrochem. Soc.* **2011**, *158*, E45–E49.

- (22) Frese, K. W. Electrochemical Reduction of CO₂ at Intentionally Oxidized Copper Electrodes. *J. Electrochem. Soc.* **1991**, *138*, 3338–3344.
- (23) Beverskoga, B.; Puigdomenech, I. Revised Pourbaix Diagrams for Copper at 25 to 300 °C. *J. Electrochem. Soc.* **1997**, *144*, 3476–3483.
- (24) Eilert, A.; Cavalca, F.; Roberts, F. S.; Osterwalder, J.; Liu, C.; Favaro, M.; Crumlin, E. J.; Ogasawara, H.; Friebe, D.; Pettersson, L. G. M.; Nilsson, A. Subsurface Oxygen in Oxide-Derived Copper Electrocatalysts for Carbon Dioxide Reduction. *J. Phys. Chem. Lett.* **2017**, *8*, 285–290.
- (25) Hong, J.; Zhang, W.; Ren, J.; Xu, R. Photocatalytic reduction of CO₂: a brief review on product analysis and systematic methods. *Anal. Methods* **2013**, *5*, 1086–1097.
- (26) Brown, T. A.; Chen, H.; Zare, R. N. Identification of Fleeting Electrochemical Reaction Intermediates Using Desorption Electrospray Ionization Mass Spectrometry. *J. Am. Chem. Soc.* **2015**, *137*, 7274–7277.
- (27) Adams, N. G.; Smith, D. The selected ion flow tube (SIFT); A technique for studying ion neutral reactions. *Int. J. Mass Spectrom. Ion Phys.* **1976**, *21*, 349–359.
- (28) Smith, D.; Diskin, A. M.; Ji, Y.; Španěl, P. Concurrent use of H₃O⁺, NO⁺, and O₂⁺ precursor ions for the detection and quantification of diverse trace gases in the presence of air and breath by selected ion-flow tube mass spectrometry. *Int. J. Mass Spectrom.* **2001**, *209*, 81–97.
- (29) Ferguson, E. E. Ion-Molecule Reactions. *Annu. Rev. Phys. Chem.* **1975**, *26*, 17–38.
- (30) Lobaccaro, P.; Mandal, L.; Motapothula, M. R.; Sherburne, M.; Martin, J.; Venkatesan, T.; Ager, J. W. Initial Application of Selected-Ion Flow-Tube Mass Spectrometry to Real-Time Product Detection in Electrochemical CO₂ Reduction. *Energy Technol.* **2017**, *6*, 110–121.
- (31) Deo, M.; Mujawar, S.; Game, O.; Yengantiwar, A.; Banpurkar, A.; Kulkarni, S.; Jog, J.; Ogale, S. Strong photo-response in a flip-chip nanowire p-Cu₂O/n-ZnO junction. *Nanoscale* **2011**, *3*, 4706–4712.
- (32) Lobaccaro, P.; Singh, M.; Clark, E. L.; Kwan, Y.; Bell, A. T.; Ager, J. W. Effects of temperature and gas-liquid mass transfer on the operation of small electrochemical cells for the quantitative evaluation of CO₂ reduction electrocatalysts. *Phys. Chem. Chem. Phys.* **2016**, *18*, 26777–26785.
- (33) Akemann, W.; Otto, A. The effect of atomic scale surface disorder on bonding and activation of adsorbates: vibrational properties of CO and CO₂ on copper. *Surf. Sci.* **1993**, *287/288*, 104–109.
- (34) Kresse, G.; Hafner, J. Ab initio molecular dynamics for liquid metals. *Phys. Rev. B: Condens. Matter Mater. Phys.* **1993**, *47*, 558–561.
- (35) Kresse, G.; Hafner, J. Ab initio molecular-dynamics simulation of the liquid-metal–amorphous-semiconductor transition in germanium. *Phys. Rev. B* **1994**, *49*, 14251–14269.
- (36) Kresse, G.; Furthmüller, J. Efficiency of ab-initio total energy calculations for metals and semiconductors using a plane-wave basis set. *Comput. Mater. Sci.* **1996**, *6*, 15–50.
- (37) Kresse, G.; Furthmüller, J. Efficient iterative schemes for ab initio total-energy calculations using a plane-wave basis set. *Phys. Rev. B: Condens. Matter Mater. Phys.* **1996**, *54*, 11169–11186.
- (38) Blöchl, P. E. Projector augmented-wave method. *Phys. Rev. B: Condens. Matter Mater. Phys.* **1994**, *50*, 17953–17979.
- (39) Kresse, G.; Joubert, D. From ultrasoft pseudopotentials to the projector augmented-wave method. *Phys. Rev. B* **1999**, *59*, 1758–1775.
- (40) Perdew, J. P.; Burke, K.; Ernzerhof, M. Generalized Gradient Approximation Made Simple. *Phys. Rev. Lett.* **1996**, *77*, 3865–3868.
- (41) Mills, G.; Jonsson, H.; Schenter, G. K. Reversible work transition state theory: application to dissociative adsorption of hydrogen. *Surf. Sci.* **1995**, *324*, 305–337.
- (42) Heyden, A.; Bell, A. T.; Keil, F. J. Efficient methods for finding transition states in chemical reactions: Comparison of improved dimer method and partitioned rational function optimization method. *J. Chem. Phys.* **2005**, *123*, 224101.
- (43) Nørskov, J. K.; Rossmeisl, J.; Logadottir, A.; Lindqvist, L.; et al. Origin of the overpotential for oxygen reduction at a fuel-cell cathode. *J. Phys. Chem. B* **2004**, *108*, 17886–17892.
- (44) Grimme, S.; Antony, J.; Ehrlich, S.; Krieg, H. A consistent and accurate ab initio parametrization of density functional dispersion correction (DFT-D) for the 94 elements H–Pu. *J. Chem. Phys.* **2010**, *132*, 154104.
- (45) Mathew, K.; Sundararaman, R.; Letchworth-Weaver, K.; Arias, T. A.; Hennig, R. G. Implicit solvation model for density-functional study of nanocrystal surfaces and reaction pathways. *J. Chem. Phys.* **2014**, *140*, 084106.
- (46) Solache-Carranco, H.; Juárez-Díaz, G.; Galván-Arellano, M.; Martínez-Juárez, J.; Romero-Paredes, G.; Peña-Sierra, R. Raman Scattering and Photoluminescence Studies on Cu₂O. *IEEE, CCE 2008*, Catalog Number: CFP08827-CDR.
- (47) Ren, X.; Rinke, P.; Scheffler, M. Exploring the random phase approximation: application to CO adsorption. *Phys. Rev. B: Condens. Matter Mater. Phys.* **2009**, *80*, 045402.
- (48) Hori, Y.; Murata, A.; Takahashi, R. Formation of hydrocarbons in the electrochemical reduction of carbon dioxide at a copper electrode in aqueous solution. *J. Chem. Soc., Faraday Trans. 1* **1989**, *85*, 2309–2326.
- (49) Peterson, A. A.; Abild-Pedersen, F.; Studt, F.; Rossmeisl, J.; Nørskov, J. K. How copper catalyzes the electroreduction of carbon dioxide into hydrocarbon fuels. *Energy Environ. Sci.* **2010**, *3*, 1311–1315.
- (50) Deng, Y.; Handoko, A. D.; Du, Y.; Xi, S.; Yeo, B. S. In Situ Raman Spectroscopy of Copper and Copper Oxide Surfaces during Electrochemical Oxygen Evolution Reaction: Identification of CuII Oxides as Catalytically Active Species. *ACS Catal.* **2016**, *6*, 2473–2481.
- (51) Chen, C. Y.; Burstein, E.; Lundquist, S. Giant Raman Scattering by Pyridine And CN Adsorbed On Silver. *Solid State Commun.* **1979**, *32*, 63–66.
- (52) Smith, B. D.; Irish, D. E.; Kedzierzawski, P.; Augustynski, J. A Surface Enhanced Raman Scattering Study of the Intermediate and Poisoning Species Formed during the Electrochemical Reduction of CO₂ on Copper. *J. Electrochem. Soc.* **1997**, *144*, 4288–4296.
- (53) Frantz, J. D. Raman spectra of potassium carbonate and bicarbonate aqueous fluids at elevated temperatures and pressures: comparison with theoretical simulations. *Chem. Geol.* **1998**, *152*, 211–225.
- (54) Dunwell, M.; Lu, Q.; Heyes, J. M.; Rosen, J.; Chen, J. G.; Yan, Y.; Jiao, F.; Xu, B. The Central Role of Bicarbonate in the Electrochemical Reduction of Carbon Dioxide on Gold. *J. Am. Chem. Soc.* **2017**, *139*, 3774–3783.
- (55) Heyes, J.; Dunwell, M.; Xu, B. CO₂ Reduction on Cu at Low Overpotentials with Surface-Enhanced in Situ Spectroscopy. *J. Phys. Chem. C* **2016**, *120*, 17334–17341.
- (56) Hori, Y.; Koga, O.; Watanabe, Y.; Matsuo, T. FTIR measurements of charge displacement adsorption of CO on poly- and single crystal (100) of Cu electrodes. *Electrochim. Acta* **1998**, *44*, 1389–1395.
- (57) Wuttig, A.; Liu, C.; Peng, Q.; Yaguchi, M.; Hendon, C. H.; Motobayashi, K.; Ye, S.; Osawa, M.; Surendranath, Y. Tracking a Common Surface-Bound Intermediate during CO₂-to-Fuels Catalysis. *ACS Cent. Sci.* **2016**, *2*, 522–528.
- (58) Dutta, A.; Kuzume, A.; Rahaman, M.; Vesztergom, S.; Broekmann, P. Monitoring the Chemical State of Catalysts for CO₂ Electroreduction: An In Operando Study. *ACS Catal.* **2015**, *5*, 7498–7502.
- (59) Calle-Vallejo, F.; Koper, M. T. M. Theoretical Considerations on the Electroreduction of CO to C₂ Species on Cu (100) Electrodes. *Angew. Chem., Int. Ed.* **2013**, *52*, 7282–7285.
- (60) Hori, Y.; Murata, A.; Tsukamoto, T.; Wakebe, H.; Koga, O.; Yamazaki, H. Adsorption of carbon monoxide at a copper electrode accompanied by electron transfer observed by voltammetry and IR spectroscopy. *Electrochim. Acta* **1994**, *39*, 2495–2648.

(61) Hori, Y.; Wakebe, H.; Tsukamoto, T.; Koga, O. Adsorption of CO accompanied with simultaneous charge transfer on copper single crystal electrodes related with electrochemical reduction of CO₂ to hydrocarbons. *Surf. Sci.* **1995**, *335*, 258–263.

(62) Nie, X.; Esopi, M. R.; Janik, M. J.; Asthagiri, A. Selectivity of CO₂ Reduction on Copper Electrodes: The Role of the Kinetics of Elementary Steps. *Angew. Chem., Int. Ed.* **2013**, *52*, 2459–2462.

(63) Akhade, S. A.; Luo, W.; Nie, X.; Bernstein, N. J.; Asthagiri, A.; Janik, M. J. Poisoning effect of adsorbed CO during CO₂ electroreduction on late transition metals. *Phys. Chem. Chem. Phys.* **2014**, *16*, 20429–20435.

(64) Lum, Y.; Ager, J. W. Stability of Residual Oxides in Oxide-Derived Cu Catalysts for Electrochemical CO₂ Reduction Investigated with 18O Labeling. *Angew. Chem., Int. Ed.* **2018**, *57*, 551–554.

(65) Lum, Y.; Yue, B.; Lobaccaro, P.; Bell, A. T.; Ager, J. W. Optimizing C–C Coupling on Oxide-Derived Copper Catalysts for Electrochemical CO₂ Reduction. *J. Phys. Chem. C* **2017**, *121*, 14191–14203.

(66) Kas, R.; Kortlever, R.; Yilmaz, H.; Koper, M. T. M.; Mul, G. Manipulating the Hydrocarbon Selectivity of Copper Nanoparticles in CO₂ Electroreduction by Process Conditions. *ChemElectroChem* **2015**, *2*, 354–358.

(67) Favaro, M.; Xiao, H.; Cheng, T.; Goddard, W. A.; Yano, J.; Crumlin, E. J. Subsurface oxide plays a critical role in CO₂ activation by Cu(111) surfaces to form chemisorbed CO₂, the first step in reduction of CO₂. *Proc. Natl. Acad. Sci. U.S.A.* **2017**, *114*, 6706–6711.

(68) Eilert, A.; Roberts, F. S.; Friebe, D.; Nilsson, A. Formation of Copper Catalysts for CO₂ Reduction with High Ethylene/Methane Product Ratio Investigated with In Situ X-ray Absorption Spectroscopy. *J. Phys. Chem. Lett.* **2016**, *7*, 1466–1470.

■ NOTE ADDED AFTER ASAP PUBLICATION

This paper was published on the Web on February 26, 2018. A new Supporting Information file with additional content was added, and the corrected version was reposted on March 1, 2018.